The Astrophysical Journal, 878:117 (12pp), 2019 June 20 https://doi.org/10.3847/1538-4357/ab204f

A New Line-by-line General Circulation Model for Simulations of Diverse Planetary Atmospheres: Initial Validation and Application to the Exoplanet GJ 1132b

Feng Ding[1] and Robin D. Wordsworth[1,2]
[1] School of Engineering and Applied Sciences, Harvard University, Cambridge, MA 02138, USA; fengding@g.harvard.edu
[2] Department of Earth and Planetary Sciences, Harvard University, Cambridge, MA 02138, USA
Received 2019 March 4; revised 2019 May 2; accepted 2019 May 7; published 2019 June 20

Abstract

Exploring diverse planetary atmospheres requires modeling tools that are both accurate and flexible. Here, we develop a three-dimensional general circulation model (3D GCM) that, for the first time, uses a line-by-line approach to describe the radiative transfer. We validate our GCM by comparing with published results done by different 1D and 3D models. To demonstrate the versatility of the model, we apply the GCM to the hot Earth-sized exoplanet GJ 1132b and study its climate and circulation assuming an atmosphere dominated by abiotic oxygen (O_2). Our simulations show that a minor CO_2 composition can change the circulation pattern substantially, intensifying the equatorial superrotation in particular. Computation of the phase-resolved spectroscopy indicates that the vertical profile of the superrotating jet could be inferred in future spectrophotometric observations by the phase shift of the hotspot in the CO_2 principle absorption band centered at 667 cm^{-1}. We also show that atmospheric mass could potentially be constrained by the phase amplitude in the O_2 vibrational fundamental band for planets with O_2-rich atmospheres, although further experimental and/or theoretical O_2–O_2 collision-induced absorption data at high temperatures is needed to confirm this. More physical schemes, such as moist dynamics, will be implemented in the GCM in the future so that it can be used to tackle a wide variety of planetary climate problems.

Key words: methods: numerical – planets and satellites: atmospheres – planets and satellites: terrestrial planets

1. Introduction

On terrestrial-mass planets, the atmospheric mass and bulk composition are expected to be extremely diverse because the external boundary conditions (particularly exchange with the planetary interior and escape to space) dominate the atmospheric evolution (Pierrehumbert 2010; Catling & Kasting 2017). The variety of planetary atmospheres in the present-day solar system is one example; the inferred evolution of the Earth's climate over geological timescales is another (Holland & Turekian 2014; Catling & Kasting 2017). For rocky planets outside the solar system, atmospheric characterization will be possible in the foreseeable future and great diversity is also expected (Birkby 2018; Madhusudhan 2018; Roberge & Seager 2018). Investigating these diverse planetary climates requires various tools, including flexible and accurate three-dimensional general circulation models (3D GCMs).

The most significant obstacle to making flexible GCMs is probably the radiative transfer calculation in a realistic, vertically inhomogeneous planetary atmosphere. Numerical computation of the radiative heating rates that drives the flow motion in GCMs is enormously computationally expensive due to the non-gray nature of the atmospheric absorption. This arises from the large number of spectral lines of the absorbing gases (exceeding billions of lines for some gases), as well as the dependence of the line absorption on the atmospheric state. As a result, statistical parameterizations of radiative transfer have previously been used to make long-term integration feasible (Stephens 1984; Goody et al. 1989; Lacis & Oinas 1991). The most popular of these tools, the correlated-*k* method, has been used for several years in studies of paleoclimate and exoplanet climates by various GCMs, including but not limited to the Laboratoire de Météorologie Dynamique Generic (LMDG) model (Wordsworth et al. 2011, 2013), the Substellar and Planetary Atmospheric Radiation and Circulation (SPARC)/MITgcm (Showman et al. 2009; Kataria et al. 2015), the Extraterrestrial Community Atmosphere Model (Wolf & Toon 2014, 2015), and the Resolving Orbital and Climate Keys of Earth and Extraterrestrial Environments with Dynamics (ROCKE-3D; Way et al. 2017). However, statistical tools have limitations, particularly when they are used outside the range for which planetary radiative transfer is well constrained by observations. Errors and biases can arise if the model is applied to a situation for which it was not designed. Just as importantly, when dealing with new temperature/pressure ranges or adding more species, a pre-processing step that relies on external line-by-line software to calculate the absorption coefficients is required. This is labor extensive and requires a careful choice of approximations, which can limit the flexibility of GCMs based on this technique.

Here we take an alternative approach to this problem and present the development of a new GCM that, for the first time, uses a line-by-line approach to calculate the radiative transfer directly. The principal advantage of this type of GCM is that our direct algorithm allows high computational accuracy and versatility when varying the atmospheric state and composition. We describe the model framework, including the line-by-line approach to calculate the radiative transfer and validation, in Section 2. As an example application, we use this GCM to simulate the possible climates on an Earth-sized exoplanet, GJ 1132b, and discuss the associated spectroscopic observable features in Section 3. Future directions of the GCM are discussed in Section 4.

2. Model Description and Validation

2.1. 1D RC Model with the Line-by-line Radiative Transfer Calculation

Before implementing the line-by-line radiative transfer calculation in the 3D GCM, we first constructed a 1D radiative–convective (RC) model. This model works in a

similar way to the conventional RC models (e.g., Manabe & Strickler 1964), except for the spectral radiative calculation. We use 2000–8000 points in the wavenumber for both shortwave and longwave calculations; as we discuss later, we tested that further increases in the spectral resolution have insignificant effects on the spectrally integrated flux and heating rates. Before performing the iteration toward the RC equilibrium state, the model first reads in the High-Resolution Transmission molecular absorption database (HITRAN) and/or the High-Temperature molecular spectroscopic database (HITEMP) line data and computes the absorption cross section at these discrete wavenumbers in a temperature–log pressure table for each absorbing species. The values of the temperature and log pressure grids are determined by the initial condition of the surface temperature and surface pressure so that the constructed table has made full use of long-term integrations. As the model iterates and the atmospheric state changes, new absorption cross sections are interpolated from this table to calculate the monochromatic optical thickness and the radiative fluxes.

Absorption cross sections are calculated by first scaling line strengths from their reference values via the formula

$$S_{ij}(T) = S_{ij}(T_0)\frac{Q(T_0)}{Q(T)}\frac{1 - e^{-h\nu_{ij}/k_B T}}{1 - e^{-h\nu_{ij}/k_B T_0}}\frac{e^{-h\nu_i/k_B T}}{e^{-h\nu_i/k_B T_0}}. \quad (1)$$

Here i and j denote the ground and excited states of the transition, respectively; S_{ij} is the line strength; ν_{ij} is the line location in frequency unit; ν_i is the ground state frequency; T is the temperature; $T_0 = 296$ K is the reference temperature; h is the Planck constant; and k_B is the Boltzmann constant (e.g., Rothman et al. 1998). Line broadening due to both collisional and Doppler effects are calculated via the usual formulae (Goody & Yung 1995). The line shapes are then calculated using the Voigt profile, with the Humlíček algorithm used to compute the complex probability function efficiently (Humlíček 1982; Schreier 1992).

A version of this model using fixed temperature profiles was first described in Schaefer et al. (2016). The time-varying RC model was presented in Wordsworth et al. (2017). To validate the 1D model, we first ensured that it reproduces analytical results when the atmosphere is gray or semi-gray. Next, for H_2O runaway greenhouse calculations, we checked that the outgoing longwave radiation (OLR) computed by our model agrees closely with published results for the Earth's atmosphere (Goldblatt et al. 2013). This inter-comparison is also discussed in Schaefer et al. (2016).

Here, for completeness, we present a summary of the model setup and describe an additional validation test we performed—a comparison among various 1D RC models with different radiative transfer calculations. The simulated case is an Earth-like planet with 1 bar pure CO_2 atmosphere orbiting the Sun at 1 au. The surface has a gray albedo of 0.20. Here the line absorption coefficients for CO_2 are calculated from the 2012 HITRAN line list (Rothman et al. 2013), and the lines are truncated at 500 cm^{-1}. The spectral range of the longwave calculation is from 1 cm^{-1} to 5 times the Wien peak wavenumber of the Planck function at the simulated surface temperature (3000 cm^{-1} in this case). Eight thousand points in the wavenumber are used so that the wavenumber increment is roughly 0.375 cm^{-1}. The CO_2 collision-induced absorption (CIA) was included using the Gruszka-Borysow-Baranov (GBB) parameterization (Gruszka & Borysow 1998; Baranov et al. 2004; Wordsworth et al. 2010). Eight quadrature points (four upwelling and four downwelling) are used for both shortwave and longwave radiative flux calculations. Currently the eight-stream radiative calculation is only performed in the pure-absorption limit. For the scattering calculation, we simply impose the enhanced reflection by Rayleigh scattering at the surface and the analytical two-stream solution is used because the molecular absorption and Rayleigh scattering occur in well-separated spectral regions. In situations where clouds or aerosols are present or when significant gas absorption extends into the visible, this approximation breaks down and a multiple scattering code is required. We will describe extensions of our model into the multiple scattering regime in subsequent papers.

We compare our 1D model to two others here for the same simulated case: the Clima model developed by Kasting and collaborators that uses the correlated-k distribution method to describe the radiative transfer (Kopparapu et al. 2013) and the linearized flux evolution (LiFE) model recently developed by Robinson & Crisp (2018) that uses a line-by-line, multiple scattering approach but combines linear flux Jacobians to rapidly adapt radiative flux profiles to changes in the atmospheric state.

A comparison of the RC equilibrium thermal structures is shown in Figure 1(a). All three models yield similar surface temperatures, and hence the vertical temperature profiles in the troposphere where dry convection occurs are also similar. One notable difference is that, in the upper atmosphere above 300 Pa, the two models with high spectral resolutions are consistent and both colder by ~10 K than the Clima model. In the troposphere and the lower stratosphere, our 1D model and the Clima model results are slightly warmer than that of the LiFE model because the LiFE model has a surface boundary scheme that allows for the temperature discontinuity from the surface to the surface air, while in most conventional 1D RC models the surface temperature is taken to be identical to the surface air temperature for simplicity. As a test, we also prescribe a surface sensible heat flux in our 1D model. When we do this, the resulting equilibrium profile is more consistent with the LiFE model in the troposphere and lower stratosphere (Figure 1(b)). As an additional test, we also compare the radiative fluxes directly computed using the radiative transfer routines adopted by these 1D models. Figure 2 compares the net solar and thermal flux profiles and the associated radiative heating rates for the same vertical temperature profile—the equilibrium thermal structure determined by the Clima model. The radiative transfer routine used by the LiFE model is the Spectral Mapping Atmospheric Radiative Transfer (SMART) model (developed by D. Crisp, see Meadows & Crisp 1996), which is a 1D multiple scattering, line-by-line radiative transfer model. Our radiative calculation agrees very well with the SMART model in the thermal infrared (IR). In the shortwave, the absorption of the atmosphere in the two models are also very similar, as shown by the slope of the net shortwave flux in Figure 2(a) and the shortwave heating rate in Figure 2(c). Our 1D model systematically underestimates the net shortwave flux by a small amount probably due to our simplification of Rayleigh scattering mentioned previously. In addition, while the Clima model systematically underestimates the net thermal radiative flux by 6 W m^{-2} above the tropopause (Figure 2(b)), the longwave cooling rate profile

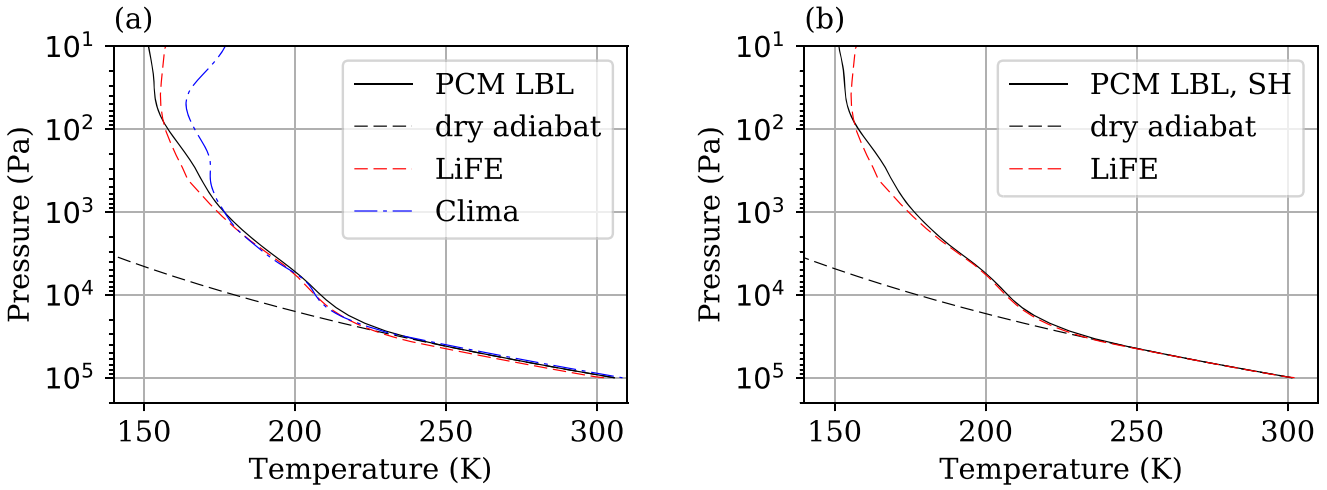

Figure 1. (a) Comparison of the equilibrium vertical temperature profiles by various models for an Earth-like planet with 1 bar pure CO_2 atmosphere (black: our 1D model, red: LiFE model, blue: Clima model). The dashed line is the dry adiabat of CO_2 with the surface temperature of our 1D model. The vertical profiles of the Clima and LiFE models are taken from Robinson & Crisp (2018). (b) Same simulation as in (a), but a surface sensible heat flux is prescribed in our 1D model (black).

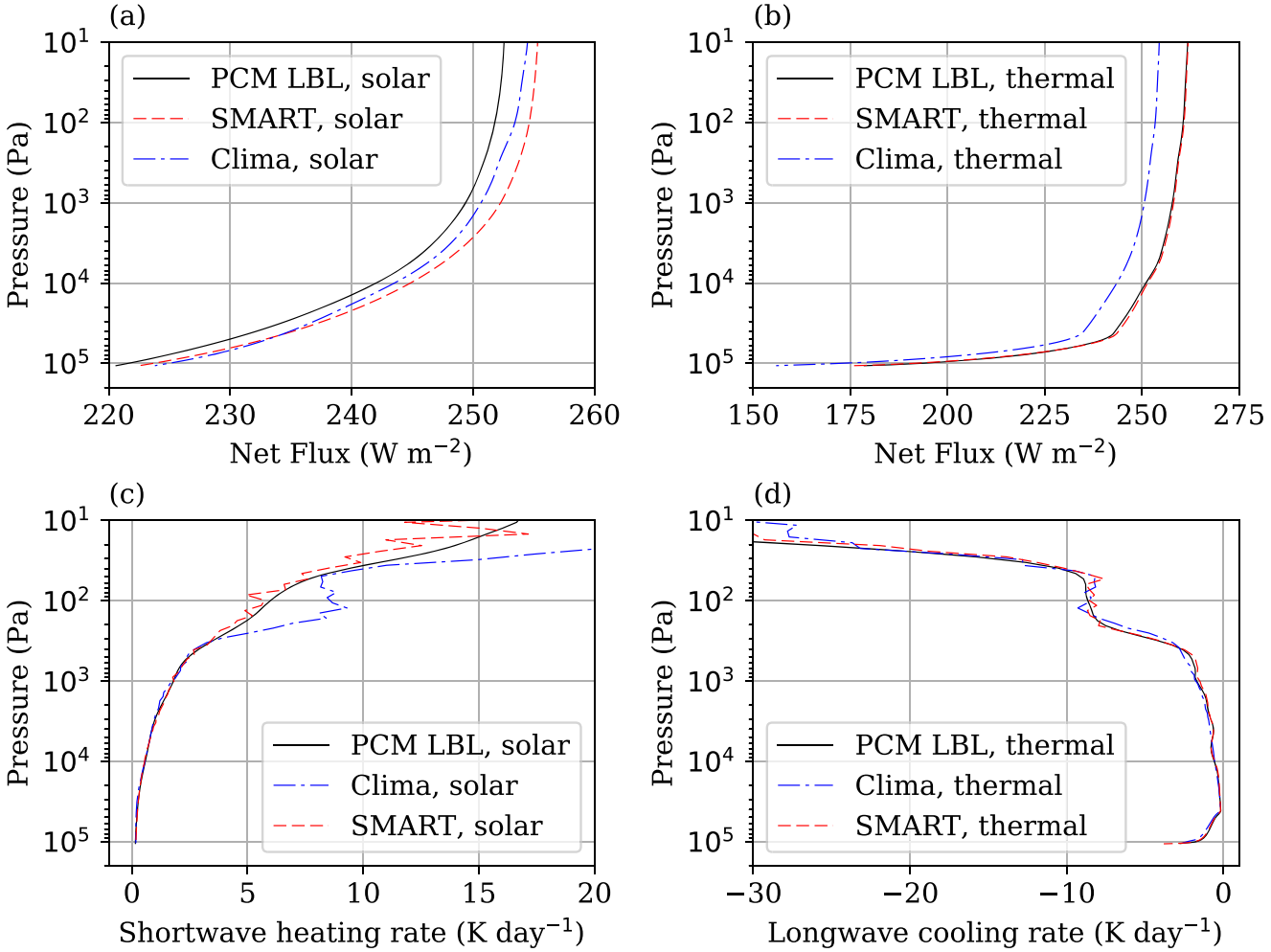

Figure 2. Vertical profiles of radiative fluxes and radiative heating rates computed with the Clima-derived equilibrium thermal structure shown in Figure 1(a) by various models (black: our 1D model, red: SMART model, blue: Clima model). (a) Net solar flux. (b) Net thermal flux. (c) Solar heating rate. (d) Thermal cooling rate.

calculated by the Clima model is very similar to the other two models, as shown in Figure 2(d). It is the strong near-IR absorption above 300 hPa that warms the upper atmosphere in the Clima model and even results in a temperature inversion above 30 hPa (Figure 1(a)). The reason for this discrepancy is unclear, but the close agreement of the two line-by-line codes suggests it is an artifact of the less accurate correlated-*k* approach taken in CLIMA.

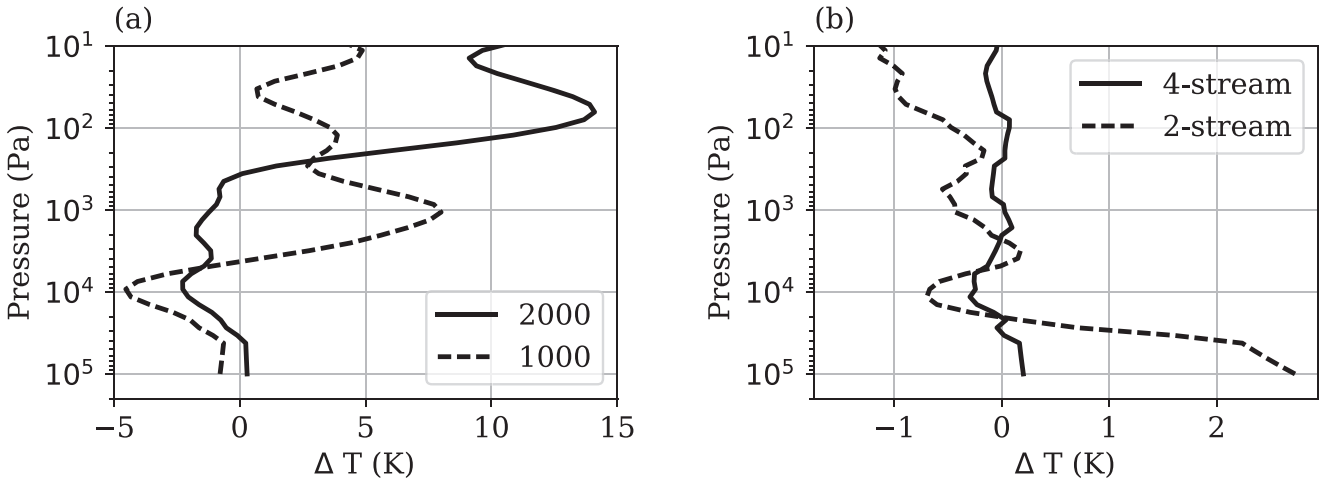

Figure 3. Difference of the temperature profiles relative to the equilibrium profile derived by our 1D model shown in Figure 1(a), which uses 8000 spectral points and eight quadrature points. (a) Same simulation as in Figure 1(a), but by our 1D model with various spectral resolutions. The numbers in the legend are the number of points in the wavenumber for each run. (b) Same simulation as in Figure 1(a), but by our 1D model with various number of quadrature points in the radiative calculation. The numbers in the legend are the number of streams for each run.

Unlike the LiFE and Clima models, which both compute the averaged radiative quantities over spectral intervals,[3] our algorithm is more like a quasi-random sampling of the absorption lines because we perform the radiative calculation at discrete regular wavenumbers, and the absorption line locations are extremely irregular (particularly for H_2O). We show the dependence of our results on spectral resolution in Figure 3(a). Interestingly, it is not necessary to use a very high spectral resolution in this radiative calculation. First, the surface temperature is very insensitive to the spectral resolution if the resolution is high enough. The surface is only warmed by 0.8 K when the number of spectral points increases from 1000 to 8000. For the upper atmosphere, which is dominated by narrow spectral bands with strong lines, a relatively high spectral resolution is necessary. For example, given 2000 spectral points, the temperature profile has relatively converged to the results with higher spectral resolutions from 300 Pa to the ground, but above 300 Pa, the cooling rate may be underestimated. Slightly more efficient results could probably be obtained using an irregular spectral grid, which is something we plan to investigate in the future. However, the convergence of the results in Figure 3(a) at 8000 points indicates the general robustness of our approach even using a regular spectral grid. Another factor that affects the radiative calculation is the number of quadrature points used to compute the radiative fluxes. Most GCMs use two-stream approximations since it is computationally efficient. In our 1D simulation, the equilibrium surface temperature rises by 2.8 K using the two-stream approach. Figure 3(b) shows that the lower atmosphere is warmed by the same degree using the two-stream approach, while a four-stream approach is sufficient in this 1 bar CO_2 atmosphere simulation.

2.2. 3D Planetary Climate Model (FMS PCM)

Our 3D GCM (hereafter referred to as FMS PCM) is developed based on the "vertically Lagrangian" finite-volume dynamical core (Lin 2004) of the Geophysical Fluid Dynamics Laboratory (GFDL) Flexible Modeling System (FMS),[4] which solves the atmospheric primitive equations in spherical coordinates. The model also includes a cubed-sphere gridding technique for atmospheric dynamics (Ronchi et al. 1996; Putman & Lin 2007), which improves both the computational performance and accuracy compared to conventional latitudinal-longitudinal gridding. For example, the cubed-sphere dynamical core allows more processors to be used for parallel computation, given the same horizontal resolution, than spectral dynamical cores in which the prognostic variables are decomposed by spherical harmonics and domain decomposition along the circles of latitude for parallel computation is not allowed. This makes the implementation of the line-by-line radiative calculation in the dynamical core feasible given modern computational resources.

The FMS dynamical core only deals with the atmospheric transport, so to build a PCM, additional physical schemes are required. The schemes we implement in FMS PCM are listed as follows:

1. Our line-by-line radiative calculation, which was introduced in Section 2.1.
2. A convection scheme. Our scheme is similar in spirit to that described in Manabe & Strickler (1964). The lapse rate in the unstable layer is adjusted toward a neutral state while conserving enthalpy. Currently the model only has a dry version, with no phase transitions of condensable substances or associated cloud formation.
3. A planetary boundary layer (PBL) scheme. The surface momentum and buoyancy fluxes are computed by the Monin–Obukhov similarity theory from the lowest level winds, temperatures, and tracer mixing ratios. A fully backward time-step method is employed for the vertical diffusion calculation in the PBL. The diffusivity is set by the *K*-profile scheme (Troen & Mahrt 1986).

To validate this 3D model, we use it to simulate the atmospheric collapse on synchronously rotating rocky planets. Our motivation for studying this setup is the simplicity of the climate dynamics—a single-component atmosphere dominated by an axisymmetric overturning circulation. We chose not to simulate the Earth's present-day climate because it is a much more complicated system. The specific case we have chosen is

[3] The averaged radiative quantities are derived based on full line-by-line calculations, and the LiFE model has a much finer spectral resolution (5 cm^{-1} in the thermal IR) than the Clima model.

[4] https://www.gfdl.noaa.gov/fms/

Table 1
Comparison of GCM Components between FMS PCM and LMD

	FMS PCM	LMD
Dynamical core	Finite volume	Finite difference
Radiation	Line-by-line	Correlated-*k* distribution
PBL diffusion	*K*-profile	Mellor–Yamada 2.5 closure

CO_2 atmosphere collapse on an Earth-like planet orbiting an M dwarf (Joshi et al. 1997; Wordsworth 2015). The detailed parameters of our simulation are given by Table 1 of Wordsworth (2015). In this simulation, the horizontal resolution is C48 ($48 \times 48 \times 6 = 13{,}824$ grid boxes in total; similar to a $2^\circ \times 2^\circ$ latitude–longitude grid); the physical schemes are performed over 26 vertical layers in the hybrid sigma-pressure coordinate. The top pressure level is 220 Pa. As shown in Figure 3(a), 2000 points in the wavenumber is enough for the radiative calculation for our setup. The equilibrium temperature profile in 1D simulations has converged to the profiles derived from higher spectral resolution runs. Therefore we reduce the spectral resolution to 2000 points in the wavenumber to save computation time. For this GCM run, we choose the two-stream approach to compute the radiative fluxes because the two-stream approach was adopted by the other GCM we will compare it with. The radiative heating rate in the GCM is updated every four model hours. With these parameters, it takes about one hour for a 200 -day integration using 384 CPU cores on our cluster. The results we present here are averages over the last 500 days of a 2000 -day integration.

The total energy conservation of a GCM is essential for climate simulations. A simple way to check it is to calculate the global-mean top-of-the-atmosphere (TOA) net radiative flux. In this run, the global-mean outgoing longwave radiative flux (OLR) is 280.28 $W\,m^{-2}$ and the outgoing shortwave radiative flux (OSR) is 61.48 $W\,m^{-2}$. Given that the global-mean insolation is the same as present Earth (341.77 $W\,m^{-2}$), net TOA radiative flux is $\sim$0.01 $W\,m^{-2}$. This also confirms that all of the physical schemes we have implemented in the GCM conserve energy very well. Our simulation agrees closely with the published result simulated by the Laboratoire de Météorologie Dynamique (LMD) Generic Model (Wordsworth 2015): the pure CO_2 atmosphere collapses on the nightside surface when the surface pressure is less than 0.1 bar. Despite the completely different components in the FMS PCM and LMD model, from the dynamical core to the grid-box physical schemes (summarized in Table 1), FMS PCM produces very similar surface temperature distributions and vertical air temperature profiles (compare Figure 4 with Figure 9 in Wordsworth 2015).

As discussed in Section 1, broadband-averaged parameterizations in radiative transfer calculations allow relatively efficient computation in conventional GCMs. But such models fail to produce flux data with sufficiently high resolution to be useful for interpretation of observations. Usually, offline radiative calculations are required to get the disk-integrated spectrum (e.g., Robinson et al. 2011). FMS PCM provides another approach to calculate the disk-integrated spectrum because a relatively high-resolution radiative calculation is performed along with the model iteration. As an example, Figure 5 shows the spectrally resolved planetary albedo and outgoing longwave radiation (OLR; spectral irradiance) in this CO_2 atmosphere collapse simulation. The left panel of Figure 5 is the spectral distribution of the global-mean planetary albedo. The Rayleigh scattering by the CO_2 atmosphere becomes significant for wavenumbers higher than 15,000 cm^{-1} and is well separated from the CO_2 absorption region, which validates our simple treatment of atmospheric scattering. The right panel of Figure 5 shows the spectral flux in the thermal IR emitted from the dayside and nightside. The IR spectroscopic feature contains very useful information regarding the vertical temperature profiles and is consistent with the profiles shown in Figure 4. On the dayside, the air temperature decreases monotonically with the height. As a result, absorption troughs emerge in the spectral region where CO_2 absorbs the thermal radiation from the lower atmosphere and re-emits it with a colder temperature. On the nightside, the absorption troughs become emission peaks because of the strong temperature inversion of the lower atmosphere. In particular, the big absorption trough in the CO_2 principal band centered at 667 cm^{-1} becomes two emission peaks due to the strong CO_2 absorption near 667 cm^{-1}. The two peak emissions on both sides of 667 cm^{-1} correspond to the temperature maximum at $\sim$4000 Pa on the nightside shown in Figure 4. Note that there is also a clear double-peak feature near 1250 cm^{-1} that is formed in a different way. It is related to the double peak of the CO_2 CIA feature (Baranov et al. 2004). The CO_2 absorption in this spectral region is much weaker than that near 667 cm^{-1}.

3. Example Application of FMS PCM: Possible Climates on an Oxidized GJ 1132b

In this section, we provide one demonstration of FMS PCM and use it to simulate the climates on a nearby exoplanet, GJ 1132b, which was recently discovered by the MEarth ground-based transiting planet survey (Berta-Thompson et al. 2015). This rocky planet has many Earth-like parameters, including the radius, surface gravity, composition, and spin rate, assuming synchronous rotation. One major difference is that GJ 1132b receives $\sim$19 times more stellar insolation than the Earth and 10 times more than Venus. Schaefer et al. (2016) discussed the possibility of abiotic O_2 buildup by the photolysis of water vapor and the subsequent atmospheric escape and mantle absorption during the magma ocean stage. The most common outcome from their simulations are tenuous atmospheres with, at most, a few bars of O_2 and little to no steam remaining. The existence of carbon- and nitrogen-bearing species is possible but is not included by the chemistry model in Schaefer et al. (2016). FMS PCM can be used to explore the possible climates on GJ 1132b with various surface pressures and atmospheric compositions. As a demonstration, we consider two simple scenarios: one with a 1 bar pure O_2 atmosphere; the other with an additional 1% CO_2. Other parameters used in the GCM simulations are listed in Table 2.

3.1. Temperature and Wind Fields

Before running any FMS PCM simulation, we need to choose the appropriate parameters for radiative transfer calculations in the GCM. Figure 6 shows some sensitivity tests. Similar to the CO_2 atmosphere collapse simulation discussed in Section 2.2, it is also not necessary to use a very high spectral resolution. For this specific case, even 1000 points in both the OLR and absorbed stellar radiation (ASR)

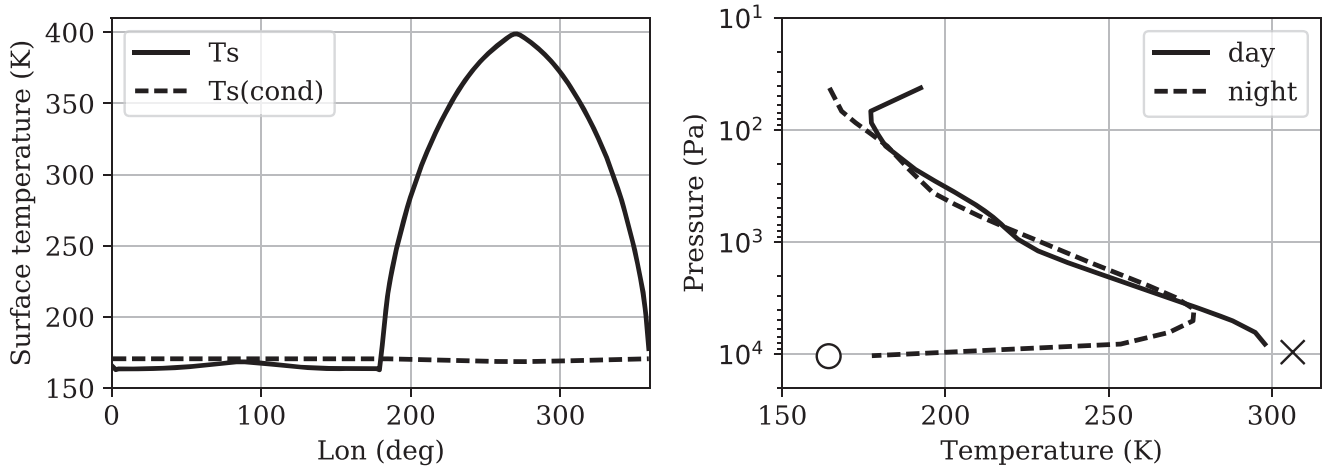

Figure 4. Left panel: equatorial surface temperature distribution (solid) and condensation temperature corresponding to the surface pressure (dashed) computed using FMS PCM for a synchronously rotating rocky planet with a pure CO_2 atmosphere. The substellar point is 270°. Right panel: hemispheric-averaged dayside (solid) and nightside (dashed) vertical temperature profiles in the same simulation. The cross and circle indicate the day and nightside surface temperatures, respectively.

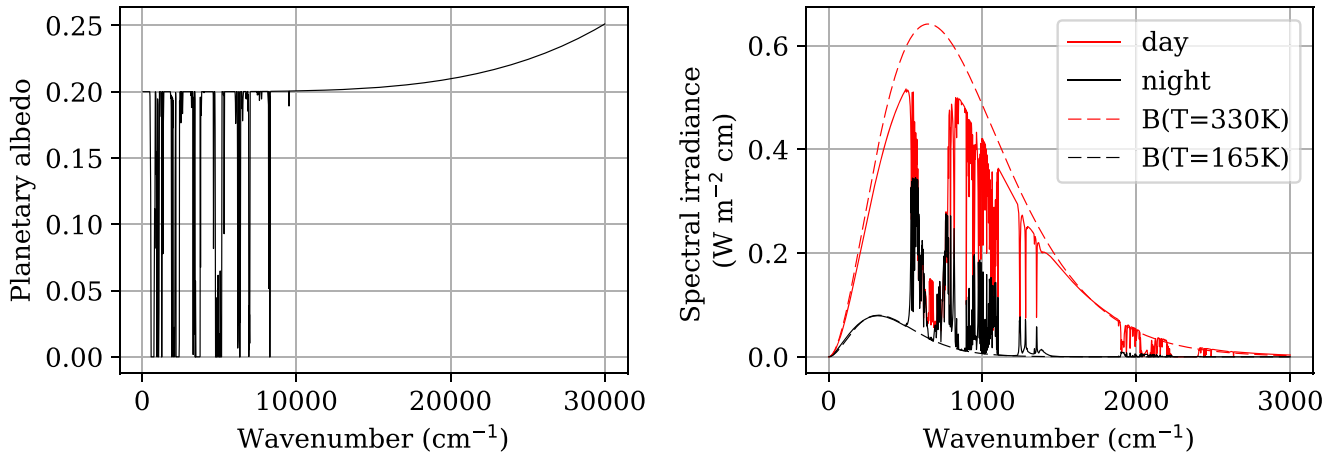

Figure 5. Left panel: spectral distribution of the global-mean planetary albedo in the same simulation shown in Figure 4. The surface has a gray albedo of 0.20. Right panel: spectral flux in the thermal IR averaged over the dayside (red solid) and the nightside (black solid). Blackbody emissions are plotted as a reference, corresponding to temperatures at 330 K (red dashed) and 165 K (black dashed). The two reference temperatures are close to the hemispheric-averaged surface temperatures.

Table 2
Parameters Used in the GCM Simulations on GJ 1132b

Parameter	Value
[a] Planet mass M ($M_\oplus$)	1.62
[a] Planet radius r ($r_\oplus$)	1.16
[a] Surface gravity g ($g_\oplus$)	1.20
[a] Orbital period P (days)	1.63
[a] Stellar flux F (1367 W m^{-2})	18.64
[b] Stellar spectrum	AD Leo
Orbital eccentricity	0.0
Obliquity	0.0
Surface roughness height (m)	5×10^{-2}
Surface albedo	0.2
Experiment A	1 bar O_2
Experiment B	1 bar O_2 + 0.01 bar CO_2

Notes.
[a] Data taken from Berta-Thompson et al. (2015).
[b] Data taken from Segura et al. (2005).

calculations yield an accuracy better than 1%, which is good enough for long-term GCM integrations. Absorption by weak lines tends to be very important in this relatively hot atmosphere. We include all CO_2 lines in the GCM runs (the minimal line strength in the HITRAN database is 10^{-30} cm^{-1}/(molecule cm^{-2})). If a line strength cutoff of 10^{-27} cm^{-1}/(molecule cm^{-2}) is applied, the OLR flux will increase by ∼1.5%.

Our simulation setup is basically the same as the CO_2 atmosphere collapse simulation in Section 2.2. The spectral resolution is also 2000 points in the wavenumber, which is an appropriate choice to maintain both computation accuracy and efficiency. However, we switch to the four-stream approach for these GCM simulations, which is more accurate than the two-stream approach, especially in the lower atmosphere (Figure 3(b)). The O_2–O_2 CIA data is calculated from the HITRAN database. The transition bands and spectral ranges are summarized in Table 1 of Richard et al. (2012). Note that for most of the bands for this data set, the temperature range is around room temperature (296 K), while the equilibrium temperature (T_{eq}) of GJ 1132b is 548 K, assuming a planetary albedo of 20%. The binary absorption coefficient does not vary linearly with the temperature, so extrapolation is not a good choice. Thus, in order to simulate radiative transfer more accurately in a O_2-rich atmosphere on such a hot planet, further

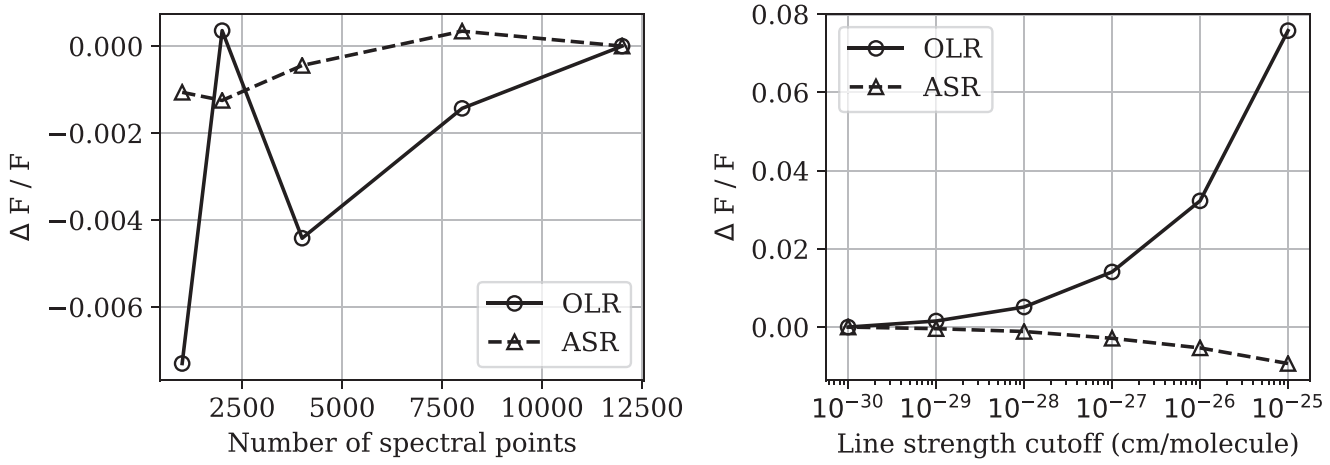

Figure 6. Relative change of radiative fluxes as a function of: (left) the number of spectral points and (right) the CO_2 line strength cutoff. The solid line with circle symbol and the dashed line with triangle symbol correspond to the OLR and the ASR, respectively. The relative change of radiative fluxes are calculated with respected to the flux with the highest resolution.

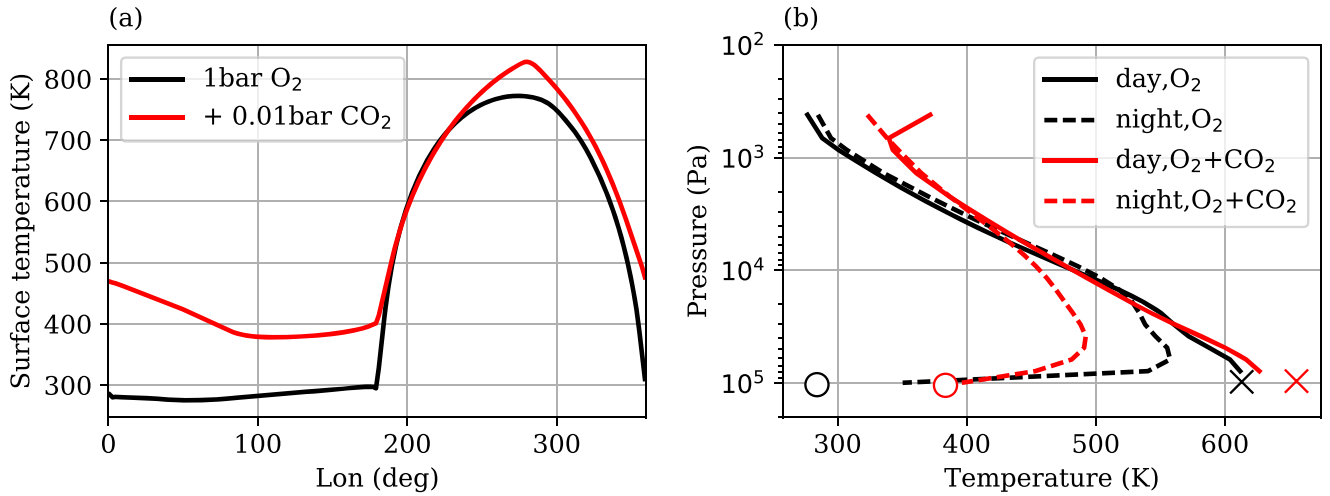

Figure 7. (a) Equatorial surface temperature distribution in the pure O_2 (black) and the O_2+CO_2 (red) simulations. The substellar point is 270°. (b) Hemispheric-averaged dayside (solid) and nightside (dashed) vertical temperature profiles in the pure O_2 (black) and the O_2+CO_2 (red) simulations. The day and nightside surface temperatures are marked by crosses and circles, respectively.

experimental and/or theoretical data at high temperatures is needed. Here we simply use the binary absorption coefficients corresponding to their highest temperatures. For this simulation, we also run the model by 2000 days and present an average result over the last 500 days.

The equatorial surface temperature distributions and vertical temperature profiles in these two experiments are shown in Figure 7. While the peak surface temperatures are much higher, the general structure here is analogous to our CO_2 collapse simulation shown in Figure 4, including the larger variations of surface temperatures on the dayside and the strong air temperature inversions in the lower atmosphere on the nightside. For the pure O_2 simulation, the upper atmosphere is much colder than the skin temperature ($T_{\rm skin} = T_{\rm eq}/2^{1/4} = 461$ K), while in 1D RC simulations (results not shown), the upper atmosphere is indeed nearly isothermal with the skin temperature due to the weak absorption by O_2. Thus the atmospheric dynamics in the GCM play a remarkable role in cooling the upper atmosphere efficiently. The energetics within a global-averaged atmospheric column can be simplified as (See Peixoto & Oort 1992 Equation (13.21))

$$\frac{\partial}{\partial p}\left[\omega\left(c_pT + gz + \frac{u^2+v^2}{2}\right)\right] = \dot{Q}_{\rm dia}, \quad (2)$$

where $\omega = Dp/Dt$ is the vertical pressure velocity, and c_pT, gz, and $(u^2+v^2)/2$ are the enthalpy, potential energy, and kinetic energy of air, respectively. $\dot{Q}_{\rm dia}$ is the diabatic heating rate, which in our GCM simulation is solely due to the radiative heating in the upper atmosphere. Because the temperature profile in this upper atmosphere deviates significantly from the radiative-equilibrium value (i.e., the skin temperature), the radiative heating rate is non-trivial and must be balanced by the convergence of vertical energy transport represented by the left-hand side of Equation (2).

Figure 7 also shows that adding 1% CO_2 to the atmosphere raises both the surface temperature and near-surface air temperature due to the greenhouse effect of CO_2. However, the lower atmosphere on the nightside is cooled because of the strong temperature inversion. CO_2 is only an IR absorber here whose radiative effect depends on the lapse rate of the

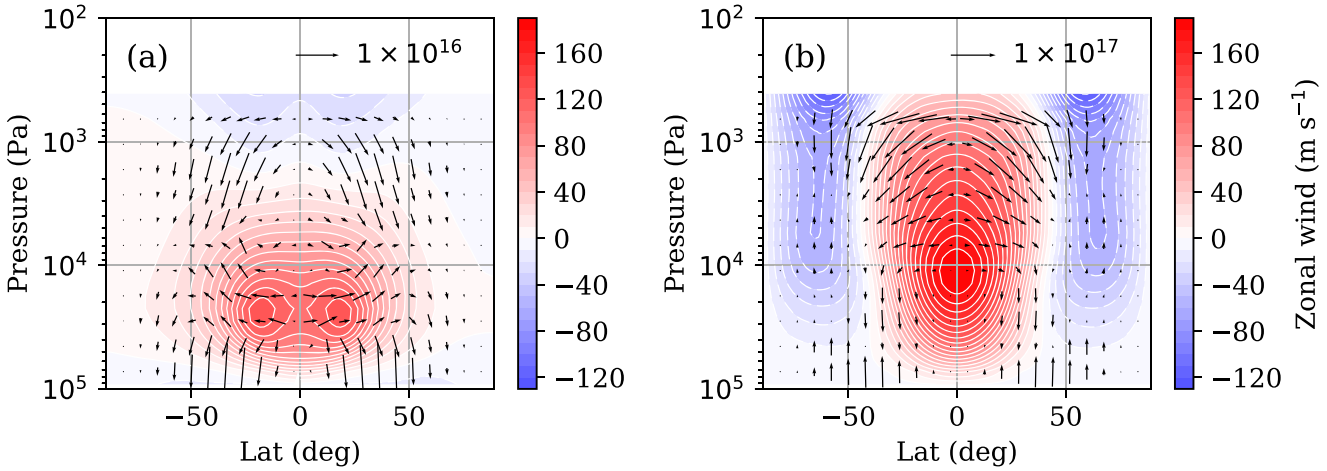

Figure 8. (a) Zonal-mean cross sections of the zonal wind component (color shading, in units of m s^{-1}) and the Eliassen–Palm flux (arrow vectors, in units of m^3 (horizontal)) for the 1 bar pure O_2 simulation. (b) Same as (a), but for the O_2+CO_2 simulation. The arrow scale for the EP flux is indicated at the top right; note that it is different in the two panels. The vertical components of the EP flux in the two panels are rescaled by a factor of $10^{-5}/\bar{p}(p)$ where $\bar{p}(p)$ is the reference density profile.

atmosphere. In other words, the surface and lower atmosphere are more closely connected by the enhanced atmospheric emissivity. A simple one-layer atmosphere model for the nightside helps to understand this effect. We assume that the surface is a blackbody with a temperature of T_s, and the overlying atmosphere has a temperature of T_a and a gray emissivity of ϵ. Ignoring the surface sensible heat exchange between the atmosphere and the surface, the energy budgets at the surface and at the top of the atmosphere are

$$\epsilon\sigma T_a^4 = \sigma T_s^4, \tag{3}$$

$$\mathrm{OLR}_n = \epsilon(2-\epsilon)\sigma T_a^4 = (2-\epsilon)\sigma T_s^4, \tag{4}$$

where σ is the Stefan–Boltzmann constant, and OLR_n is the mean outgoing longwave radiation on the nightside that also equals to the heat transport from the dayside to the nightside. First, Equation (3) shows that for a gray atmosphere ($\epsilon < 1$), $T_a > T_s$ and the temperature inversion is necessary on the nightside. Then we can see that an increase of the atmospheric emissivity tends to warm the surface and cool the overlying atmosphere, assuming a small change in the OLR_n from Equation (4) (see also Section 3.3 of Wordsworth 2015 for a similar analysis assuming a uniform atmospheric temperature). However, the change of the temperature in the GCM runs is much more complicated than this simple model with these assumptions. First, more energy is transported to the nightside in the O_2+CO_2 run. Second, the surface sensible heat is comparable to the radiative fluxes. Third, the atmosphere is not gray but only absorbs the infrared radiation strongly in some spectral regions by CO_2. Our qualitative explanation here does not take these effects into account. Koll & Abbot (2016) developed a two-column RC-subsiding model to study temperature structures of dry tidally locked rocky exoplanets, which incorporates the atmospheric dynamics by constraining the large-scale wind speed using heat engine efficiency. Figure 10 in Koll & Abbot (2016) shows similar results to our GCM simulations: an increase in the longwave optical thickness warms the nightside surface but cools the nightside overlying atmosphere, when the atmosphere is not optically thick and has a small wave-to-radiative timescale ratio (for our GCM runs on GJ 1132b, it is ∼0.04).

Note that GJ 1132b has an Earth-like spin rate assuming synchronous rotation. The effects of planetary rotation on the atmospheric circulation becomes significant compared to our CO_2 collapse simulation shown in Figure 4. We can verify this by comparing the planetary radius with the equatorial Rossby deformation radius $L_{\mathrm{RO}}^2 \sim (\sqrt{\mathrm{RT_{eq}}}/\Omega a)a^2$, where R is the specific gas constant, T_{eq} is the equilibrium temperature, Ω is the spin rate of the planet, and a is the planetary radius (e.g., Koll & Abbot 2015; Pierrehumbert & Ding 2016). The non-dimensional parameter $(\sqrt{\mathrm{RT_{eq}}}/\Omega a)$ for GJ 1132b is 1.14. As a comparison, this parameter is 0.62 for the Earth and 18 for our CO_2 collapse simulation. As a consequence of planetary wave perturbations, the symmetry of the surface temperature around the substellar (270°) and antistellar point (90°) in Figure 4 breaks down in the two GJ 1132b simulations, as shown in Figure 7(a).

Another consequence of the planetary wave perturbations is equatorial superrotation. The zonal-mean cross sections of the zonal wind are plotted in Figure 8. Equatorial superrotation is a common feature of hot-Jupiter simulations with speeds of 1–4 km s^{-1} (Showman & Guillot 2002; Dobbs-Dixon & Lin 2008; Menou & Rauscher 2009). It has also been observed indirectly by the eastward displacement of the hottest region from the substellar point in light curves of the hot Jupiter HD 189733b (Knutson et al. 2007) and by the the ellipsoidal/beaming amplitude discrepancy on Kepler-76b (Faigler et al. 2013). The equatorial superrotating jets in the two experiments are of the order of 100 m s^{-1}, which is much slower than the simulated jet speed on hot Jupiters, probably because of the efficient surface momentum dissipation and the heavier molecular weight of the O_2 atmosphere compared to the H_2-dominated atmosphere on hot Jupiters. The effects of molecular weight on the zonal wind speed was discussed in Zhang & Showman (2017). To illustrate the underlying mechanism of equatorial superrotation, we calculated the Eliassen–Palm (EP) flux in the latitude-pressure coordinate, which is a useful tool for diagnostics of wave activities in the Earth's climate (e.g., Edmon et al. 1980). The horizontal and vertical components of the EP flux relate to the meridional eddy

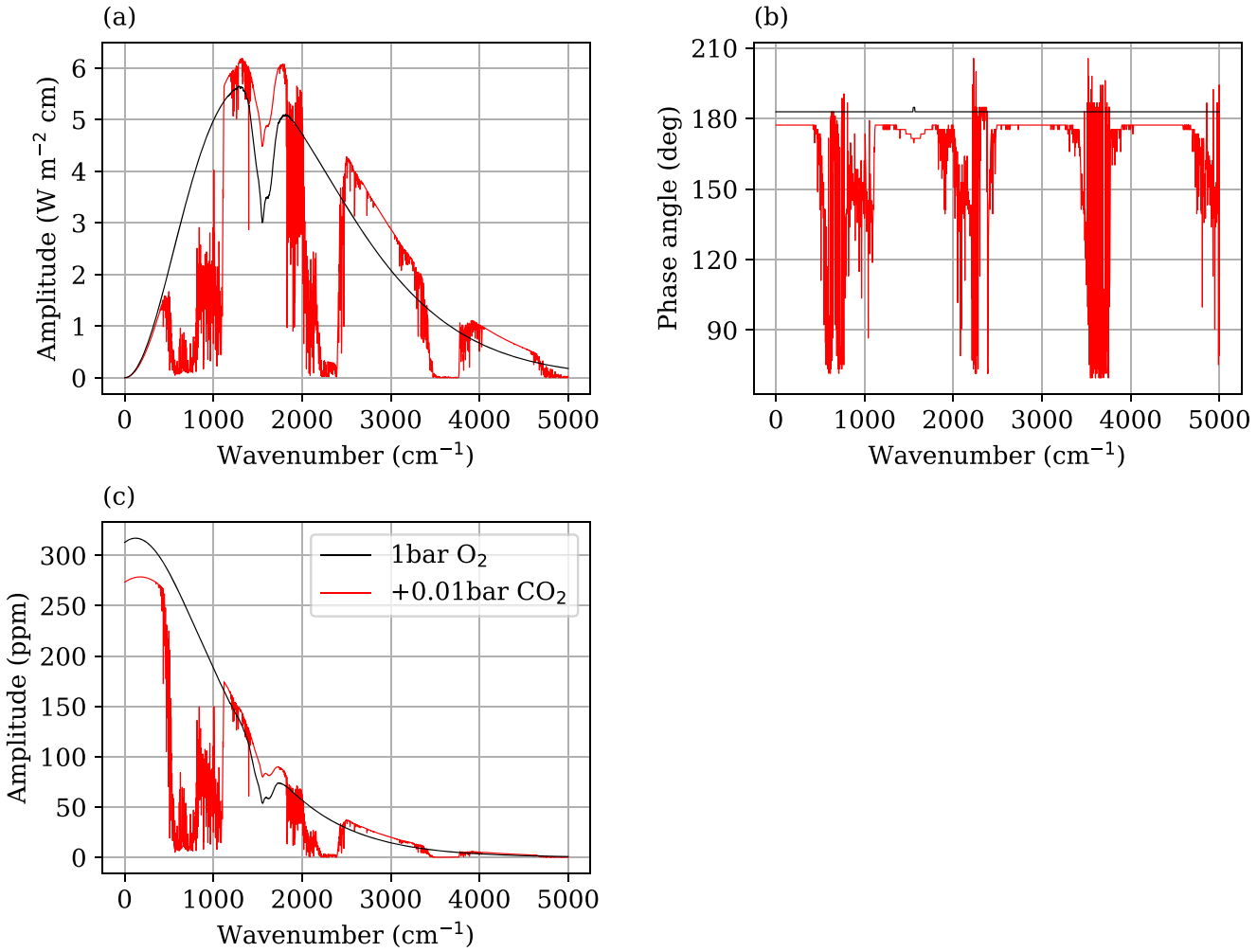

Figure 9. Spectral distribution of the thermal phase curve in the 1 bar pure O_2 (black) and the O_2+CO_2 (red) simulation: (a) the amplitude ("variation spectrum" following Selsis et al. 2011), (b) the phase angle corresponding to the highest emission, and (c) same as (a) but taking into account the star–planet contrast. The phase amplitude is expressed in ppm.

momentum and the heat flux in the atmosphere, respectively. The divergence of the EP flux represents an internal forcing of the zonal jet by disturbances, so that the equatorial superrotation in Figure 8 can be explained by the divergence of the vectors at the equator. Comparing the two panels in Figure 8 shows that adding 1% of CO_2 to the atmosphere changes the circulation pattern substantially. It amplifies the contrast of the radiative-equilibrium temperature between the dayside and nightside, and therefore increases the wave amplitude and the equatorial superrotating jet speed. More angular momentum is transported equatorward from high latitudes, creating two easterly jets above 50°. The position of the jet core also changes. In the pure O_2 simulation, two jet cores form in the subtropics associated with the meridional mean angular momentum transport, although the air above the equator still superrotates. With an additional 1% CO_2, one well-formed jet core is found at 0.1 bar above the equator.

3.2. Thermal Phase Curves

Thermal phase curves, which are the variations of the apparent IR emission of an planet with its orbital phase, have been observed for hot Jupiters and used to infer their temperature distribution and atmospheric circulation (e.g., Knutson et al. 2007). Furthermore, Selsis et al. (2011) addressed the ability to use the multiband phase curves to characterize the atmosphere on hot terrestrial exoplanets with next-generation observations. Here we compute the disk-integrated and observer-projected spectrum from GJ 1132b following Cowan & Agol (2008) and Koll & Abbot (2015, Appendix C) for $F_\nu(\theta)$ where θ is the phase angle (we assume $\theta = 0°$ at primary transit and $\theta = 180°$ at secondary eclipse). Then we plot the spectral distribution of the amplitude of $F_\nu(\theta)$ and the phase angle corresponding to the highest emission $\theta_{\max}$ in Figures 9(a) and (b), respectively. Note that $F_\nu(\theta)$ here is the disk-integrated and observer-projected flux from the planet. Then the star–planet contrast seen by a distant observer should be $F_\nu r_p^2 / F_{\nu,*} r_*^2$, where $F_{\nu,*}$ is the spectral flux from the M dwarf GJ 1132 at the same wavenumber, and r_p and r_* are the radius of the planet GJ 1132b and the star GJ 1132, respectively.

The spectral distribution of the amplitude of $F_\nu(\theta)$ is called the "variation spectrum" in Selsis et al. (2011). In our simulations, it has a similar shape to the emission spectrum from the dayside atmosphere (e.g., Figure 5) because the temperature contrast between the dayside and nightside atmosphere decreases with the height (shown in Figure 7(b)) and window regions exhibit larger variations than optically thick spectral regions. Meadows (2017) performed a thorough

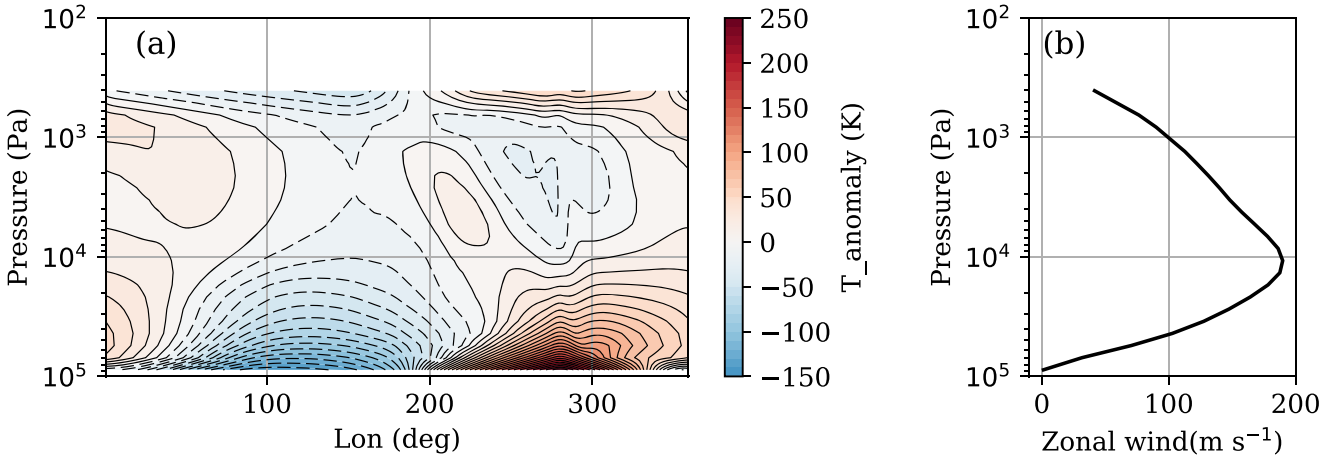

Figure 10. (a) Vertical cross section of the air temperature anomaly (obtained by subtracting the zonal mean) along the equator in the O_2+CO_2 simulation. The substellar point is 270°. (b) Vertical profile of the zonal-mean zonal wind speed at the equator. The longitudinal tilting of the hotspot correlates well with the superrotating jet.

review on the identification of an oxygenic photosynthetic biosphere and discrimination between biological and abiotic sources of O_2, but only with a focus on transmission spectroscopy and direct imaging of exoplanets. As described in Selsis et al. (2011), the variation spectrum is an interesting possibility for molecular signature detections. In our simulations, O_2 absorption in the variation spectrum is significant in its vibrational fundamental band near 1500 cm^{-1}. Figure 9(c) also shows the spectral distribution of the phase amplitude, taking into account the star–planet contrast. The signal near 400 cm^{-1} is ∼300 ppm, which is slightly smaller than the day–night thermal emission contrast of a bare rock GJ 1132b in the mid-IR (373 ppm, Koll & Abbot 2016) because of the heat redistribution in the GCM simulation. We estimate the precision of the *James Webb Space Telescope* (*JWST*) in the mid-IR (6.6–8.8 μm broad band, F770W on the Mid-Infared Instrument, MIRI) assuming photon noise following Koll & Abbot (2016). The imperfect instrument throughput is accounted for by a factor of one-third (Figure 3; Glasse et al. 2010). For one full orbit integration, the 1σ uncertainty interval for the phase amplitude is 7 ppm. The O_2 absorption in this band reduces the flux ratio by ∼20 ppm compared to the bare rock scenario. The value is much smaller in the O_2+CO_2 simulation, as Figure 9(c) shows, which is probably associated with the enhanced near-surface temperature inversion on the nightside described in Section 3.1. Therefore our simulations indicate that if the O_2-dominated atmosphere is thinner than 1 bar, it might be difficult to distinguish from a bare rock case using the IR phase curves.

Other than the amplitude of the phase curve, our calculation indicates that the spectral distribution of the phase angle corresponding to the highest emission θ_{max} can also be used for molecular detections. Moreover the θ_{max} distribution provides valuable information regarding the vertical profile of the hotspot shift in the atmosphere, which is associated with atmospheric dynamics. In the 1 bar pure O_2 simulation, θ_{max} in the O_2 fundamental band indicates that there is insignificant hotspot shift in the lower atmosphere relative to the surface. In the O_2+CO_2 simulation, θ_{max} in the same band indicates a 6° eastward shift of the lower atmosphere hotspot, as a result of the circulation change discussed in Section 3.1. The absorption bands of CO_2 have more complicated features. We can take the principle absorption band centered at 667 cm^{-1} as an example. In both the window region with little absorption and the optically thick region near the 667 cm^{-1} center, $\theta_{max} \sim 180°$, indicating small hotspot shifts at the surface and the top of the atmosphere. But on the shoulder of this absorption band, θ_{max} can be as low as 75°, indicating a significant eastward shift of the hotspot by 105° in the middle atmosphere.

Figure 10(a) shows the vertical cross section of the air temperature anomaly (obtained by subtracting the zonal mean) along the equator in the O_2+CO_2 simulation to confirm our inferences from the θ_{max} distribution. There is a remarkable eastward shift of the hotspot in the middle atmosphere near 10^4 Pa, which is also the altitude of the jet core shown in Figure 8(b). Moreover the longitudinal tilting of the hotspot correlates well with this equatorial superrotating jet because the hotspot shift is the consequence of atmospheric dynamics. Previous studies suggested that the eastward hotspot shift is caused by the equatorial superrotating jet (e.g., Zhang & Showman 2017; Hammond & Pierrehumbert 2018), with Zhang & Showman (2017) focusing on the heat advection by the equatorial superrotating jet and Hammond & Pierrehumbert (2018) focusing on the Doppler-shifting stationary wave response. Note that, until now, theoretical work has only been done in the shallow-water framework. Further investigation is needed to explore whether baroclinicity is important for wave-mean flow interactions and therefore the longitudinal tilting of the hotspot in this situation of large horizontal temperature variation.

4. Discussion

We described a new 3D climate model, FMS PCM, which uses a line-by-line approach to describe the radiative transfer. We validated our radiation code when the absorbing species are H_2O and CO_2. At present, the same number of spectral points are used for both shortwave and longwave calculation and are evenly spaced. For other absorbing species that have a narrow absorption spectral region or relatively regular line positions (e.g., CO), we may need adaptive spectral grids and make the radiative calculation more efficient. We plan to investigate this in the future.

Before running the GCM, some preparation is required to determine the appropriate setup (most importantly, the spectral resolution) and to maintain the computational accuracy and

efficiency for long-term integrations. Compared to conventional GCMs that use parameterized radiative calculations, however, our model is designed to be both more accurate and flexible for the study of diverse planetary atmospheres. Moreover because all spectral quantities are calculated within FMS PCM, this model can help interpret next-generation exoplanet observations. For example, we show that the emission spectrum in the CO_2 principle absorption band centered at 667 cm^{-1} could be used to infer the near-surface temperature inversion on the nightside of tidally locked terrestrial planets.

We used FMS PCM to study a possible O_2-dominated atmosphere on GJ 1132b. Currently the atmospheric composition of this planet is very poorly constrained, and so future studies should explore the dynamical and climate implications of a wider range of possibilities. The simulation results show that a minor amount of CO_2 in the atmosphere can change the climate substantially, notably by enhancing the near-surface temperature inversion on the nightside and intensifying the equatorial superrotation and high-latitude easterlies. Moreover the vertical profile of the equatorial superrotation could be inferred from the phase shift in the CO_2 principle absorption band centered at 667 cm^{-1}. As an example of using GCM simulations to help interpret exoplanet atmospheric observations, the metallicity of a hot Jupiter, WASP-43b, was constrained in a study by Kataria et al. (2015) by comparing a range of GCM results to the *Hubble Space Telescope* (*HST*)/Wide Field Camera 3 spectrophotometric phase curve measurements. While the phase-resolved spectroscopic feature on GJ 1132b we discussed here lies in the mid-IR rather than the visible/near-IR, it should be possible to perform such measurements using next-generation instruments, such as *JWST* (Selsis et al. 2011; Beichman et al. 2014; Cowan et al. 2015; Koll & Abbot 2016). Koll & Abbot (2016) estimated the amount of time required to measure the thermal phase curves of short-period terrestrial planets with *JWST*/MIRI, which is similar to the time required to detect molecules via stacked transit spectroscopy. Although, in our GCM simulations with 1 bar O_2, the molecular O_2 absorption is hard to identify in its fundamental band near 1500 cm^{-1} due to a small signal-to-noise ratio (S/N), a large S/N is still expected for thicker O_2 atmospheres. The broadband IR phase amplitude can be used to constrain the atmospheric mass, as suggested by Koll & Abbot (2015). Note that the O_2–O_2 CIA data in the vibrational fundamental band is only measured below 360 K, and the temperature dependence is very nonlinear (Baranov et al. 2005). Further experimental and/or theoretical data at high temperatures is required to improve the radiative calculation at high temperatures.

So far FMS PCM is only a dry model. Moist dynamics, including phase transitions of condensible substances and formation and transport of condensates, is not yet implemented. In the future, we also plan to extend the radiative transfer model to allow for full treatment of multiple scattering by atmospheric particulates (clouds and hazes). Nonetheless the dry runs discussed in this paper demonstrate the high potential of this approach. We believe that this new type of GCM model will allow for the detailed study of a wide variety of important planetary climate problems in the future, including the climate dynamics of condensible-rich atmospheres (Ding & Pierrehumbert 2016, 2018; Pierrehumbert & Ding 2016), atmospheric characterization of exoplanets near the inner and outer edges of the habitable zone (Wordsworth et al. 2011; Yang et al. 2013; Kopparapu et al. 2016), and water loss and abiotic oxygen buildup in water-rich atmospheres (Wordsworth & Pierrehumbert 2014).

Support for this work was provided by NASA grants NASA NNX16AR86G and 80NSSC18K0829. The GCM simulations in this paper were carried out on the Odyssey cluster supported by the FAS Division of Science, Research Computing Group at Harvard University. The authors would like to thank Tyler D. Robinson for insightful comments on this work and for facilitating model comparisons with the Clima and LiFE model and Wanying Kang and Hannah Diamond-Lowe for helpful discussions.

ORCID iDs

Feng Ding https://orcid.org/0000-0001-7758-4110

References

Baranov, Y. I., Lafferty, W. J., & Fraser, G. T. 2004, JMoSp, 228, 432
Baranov, Y. I., Lafferty, W. J., & Fraser, G. T. 2005, JMoSp, 233, 160
Beichman, C., Benneke, B., Knutson, H., et al. 2014, PASP, 126, 1134
Berta-Thompson, Z. K., Irwin, J., Charbonneau, D., et al. 2015, Natur, 527, 204
Birkby, J. L. 2018, Handbook of Exoplanets (Cham: Springer), 16
Catling, D. C., & Kasting, J. F. 2017, Atmospheric Evolution on Inhabited and Lifeless Worlds (Cambridge: Cambridge Univ. Press)
Cowan, N. B., & Agol, E. 2008, ApJL, 678, L129
Cowan, N. B., Greene, T., Angerhausen, D., et al. 2015, PASP, 127, 311
Ding, F., & Pierrehumbert, R. T. 2016, ApJ, 822, 24
Ding, F., & Pierrehumbert, R. T. 2018, ApJ, 867, 54
Dobbs-Dixon, I., & Lin, D. N. C. 2008, ApJ, 673, 513
Edmon, H. J., Jr., Hoskins, B. J., & McIntyre, M. E. 1980, JAtS, 37, 2600
Faigler, S., Tal-Or, L., Mazeh, T., Latham, D. W., & Buchhave, L. A. 2013, ApJ, 771, 26
Glasse, A. C. H., Bauwens, E., Bouwman, J., et al. 2010, Proc. SPIE, 7731, 77310K
Goldblatt, C., Robinson, T. D., Zahnle, K. J., & Crisp, D. 2013, NatGe, 6, 661
Goody, R., West, R., Chen, L., & Crisp, D. 1989, JQSRT, 42, 539
Goody, R., & Yung, Y. 1995, Atmospheric Radiation: Theoretical Basis (Oxford: Oxford Univ. Press)
Gruszka, M., & Borysow, A. 1998, MolPh, 93, 1007
Hammond, M., & Pierrehumbert, R. T. 2018, ApJ, 869, 65
Holland, H., & Turekian, K. 2014, Treatise on Geochemistry Vol. 6 (Amsterdam: Elsevier)
Humlíček, J. 1982, JQSRT, 27, 437
Joshi, M. M., Haberle, R. M., & Reynolds, R. T. 1997, Icar, 129, 450
Kataria, T., Showman, A. P., Fortney, J. J., et al. 2015, ApJ, 801, 86
Knutson, H. A., Charbonneau, D., Allen, L. E., et al. 2007, Natur, 447, 183
Koll, D. D. B., & Abbot, D. S. 2015, ApJ, 802, 21
Koll, D. D. B., & Abbot, D. S. 2016, ApJ, 825, 99
Kopparapu, R. K., Ramirez, R., Kasting, J. F., et al. 2013, ApJ, 765, 131
Kopparapu, R. k., Wolf, E. T., Haqq-Misra, J., et al. 2016, ApJ, 819, 84
Lacis, A. A., & Oinas, V. 1991, JGR, 96, 9027
Lin, S.-J. 2004, MWRv, 132, 2293
Madhusudhan, N. 2018, Handbook of Exoplanets (Cham: Springer), 104
Manabe, S., & Strickler, R. F. 1964, JAtS, 21, 361
Meadows, V. S. 2017, AsBio, 17, 1022
Meadows, V. S., & Crisp, D. 1996, JGR, 101, 4595
Menou, K., & Rauscher, E. 2009, ApJ, 700, 887
Peixoto, J. P., & Oort, A. H. 1992, Physics of Climate (New York: AIP)
Pierrehumbert, R. T. 2010, Principles of Planetary Climate (Cambridge: Cambridge Univ. Press)
Pierrehumbert, R. T., & Ding, F. 2016, RSPSA, 472, 20160107
Putman, W. M., & Lin, S.-J. 2007, JCoPh, 227, 55
Richard, C., Gordon, I. E., Rothman, L. S., et al. 2012, JQSRT, 113, 1276
Roberge, A., & Seager, S. 2018, Handbook of Exoplanets (Cham: Springer), 98
Robinson, T. D., & Crisp, D. 2018, JQSRT, 211, 78
Robinson, T. D., Meadows, V. S., Crisp, D., et al. 2011, AsBio, 11, 393
Ronchi, C., Iacono, R., & Paolucci, P. S. 1996, JCoPh, 124, 93
Rothman, L. S., Gordon, I. E., Babikov, Y., et al. 2013, JQSRT, 130, 4
Rothman, L. S., Rinsland, C. P., Goldman, A., et al. 1998, JQSRT, 60, 665

Schaefer, L., Wordsworth, R. D., Berta-Thompson, Z., & Sasselov, D. 2016, ApJ, 829, 63
Schreier, F. 1992, JQSRT, 48, 743
Segura, A., Kasting, J. F., Meadows, V., et al. 2005, AsBio, 5, 706
Selsis, F., Wordsworth, R. D., & Forget, F. 2011, A&A, 532, A1
Showman, A. P., Fortney, J. J., Lian, Y., et al. 2009, ApJ, 699, 564
Showman, A. P., & Guillot, T. 2002, A&A, 385, 166
Stephens, G. L. 1984, MWRv, 112, 826
Troen, I. B., & Mahrt, L. 1986, BoLMe, 37, 129
Way, M. J., Aleinov, I., Amundsen, D. S., et al. 2017, ApJS, 231, 12
Wolf, E. T., & Toon, O. B. 2014, AsBio, 14, 241
Wolf, E. T., & Toon, O. B. 2015, JGRD, 120, 5775
Wordsworth, R. 2015, ApJ, 806, 180
Wordsworth, R., Forget, F., & Eymet, V. 2010, Icar, 210, 992
Wordsworth, R., Forget, F., Millour, E., et al. 2013, Icar, 222, 1
Wordsworth, R., Kalugina, Y., Lokshtanov, S., et al. 2017, GeoRL, 44, 665
Wordsworth, R., & Pierrehumbert, R. 2014, ApJL, 785, L20
Wordsworth, R. D., Forget, F., Selsis, F., et al. 2011, ApJL, 733, L48
Yang, J., Cowan, N. B., & Abbot, D. S. 2013, ApJL, 771, L45
Zhang, X., & Showman, A. P. 2017, ApJ, 836, 73